

Deep Learning Inversion of Electrical Resistivity Data

Bin Liu, Qian Guo, Shucai Li, Benchao Liu, Yuxiao Ren, Yonghao Pang, Lanbo Liu,
and Peng Jiang, *Member, IEEE*

Abstract—The inverse problem of electrical resistivity surveys (ERS) is difficult because of its nonlinear and ill-posed nature. For this task, traditional linear inversion methods still face challenges such as sub-optimal approximation and initial model selection. Inspired by the remarkable non-linear mapping ability of deep learning approaches, in this paper we propose to build the mapping from apparent resistivity data (input) to resistivity model (output) directly by convolutional neural networks (CNNs). However, the vertically varying characteristic of patterns in the apparent resistivity data may cause ambiguity when using CNNs with the weight sharing and effective receptive field properties. To address the potential issue, we supply an additional tier feature map to CNNs to help it get aware of the relationship between input and output. Based on the prevalent U-Net architecture, we design our network (ERSInvNet) which can be trained end-to-end and reach real-time inference during testing. We further introduce depth weighting function and smooth constraint into loss function to improve inversion accuracy for the deep region and suppress false anomalies. Four groups of experiments are considered to demonstrate the feasibility and efficiency of the proposed methods. According to the comprehensive qualitative analysis and quantitative comparison, ERSInvNet with tier feature map, smooth constraints and depth weighting function together achieve the best performance.

Index Terms—Electrical resistivity inversion, Deep learning.

I. INTRODUCTION

Electrical resistivity survey (ERS), as one of the most well-known and commonly applied investigation technologies (Loke *et al.* [1]), has been widely used in environmental investigations (LaBrecque *et al.* [2], Hayley *et al.* [3], Reynolds [4]), engineering prospecting (Kim *et al.* [5], Wilkinson *et al.* [6], Sjodahl *et al.* [7]), hydrological surveys (Park [8]; Slater and Binley [9], Rucker [10], Cho *et al.* [11]) and mining applications (Legault *et al.* [12], Chambers *et al.* [13], Liu *et al.* [14]). Geological interpretations using observed data are usually far from revealing the complex characteristics of subsurface properties. Thus, to satisfy geological interpretation purposes, geophysical inversion methods are continually focused on reconstructing more accurate and detailed subsurface properties.

After years of development, nonlinear optimization methods have been widely adopted in ERS inverse problems, such as Genetic Algorithm (Schwarzbach *et al.* [15], Liu *et al.* [16]), Simulated Annealing Algorithm (Sharma and

Kaikkonen [17]), Particle Swarm Optimization (PSO) (Shaw and Srivastava [18]). Particularly, instead of optimizing resistivity model, Artificial Neural Networks (ANNs) build the mapping between apparent resistivity data and resistivity model directly by updating parameters of networks. With ANNs, some significant results in ERS inversion have been gained in both synthetic and field tests (El-Qady and Ushijima [19], Neyamadpour *et al.* [20], Maiti *et al.* [21], Jiang *et al.* [22]). Usually, ANNs are optimized by gradients derived from loss functions. Due to the gradient vanish/explosion problems, it is not easy to train a deep and large ANNs with strong modeling capacity at the beginning. Thus, some limitations such as slow convergence, low accuracy and over-fitting phenomenon in training remain (Al-Abri and Hilal [23]).

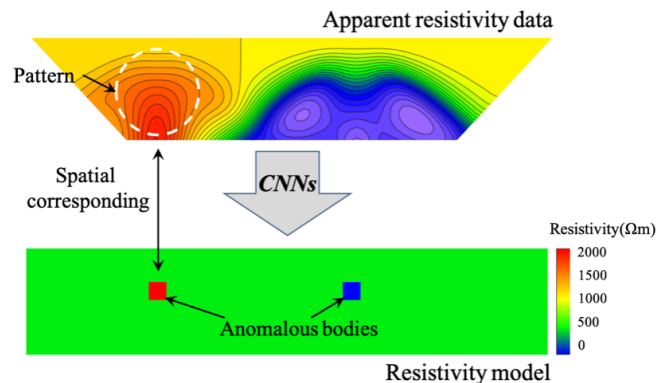


Fig. 1. Task definition. Observed data caused by different resistivity anomalies in the model show different patterns in apparent resistivity pseudosection, and the patterns show certain spatial correspondence to resistivity anomalies.

Recently, many approaches are proposed to help back-propagate gradients efficiently through the whole networks, such as residual units proposed by He *et al.* [24], activation functions proposed by Maas *et al.* [25] and normalization layer proposed by Ioffe and Szegedy [26]. With them, ANNs with deep layers and tremendous parameters could be optimized. Accordingly, people tend to refer to deep Artificial Neural Networks (ANNs) as Deep Neural Networks (DNNs). Methods based on DNNs are usually called deep learning which has shown superior performance in many problems that require the perception and decision abilities of machines (LeCun *et al.* [27]). Originally succeeding in computer vision for the tasks of image perception (*e.g.*, Krizhevsky *et al.* [28], Simonyan and Zisserman [29], He *et al.* [24], Jiang *et al.* [30], etc.), now DNNs have been prevalent in many fields such as computer graphics, natural language processing (NLP).

Corresponding author: Peng Jiang.

B. Liu, G. Qian, S. Li, B. Liu, Y. Ren, Y. Pang and P. Jiang are with Shandong University, China. (Emails: liubin0635@163.com; hhu_gq@163.com; lishucai@sdu.edu.cn; sdujubenchao@163.com; ryxchina@gmail.com; yonghao_pang@163.com and sdujump@gmail.com). L. Liu is with University of Connecticut, USA. (Email: lanbo.liu@uconn.edu)

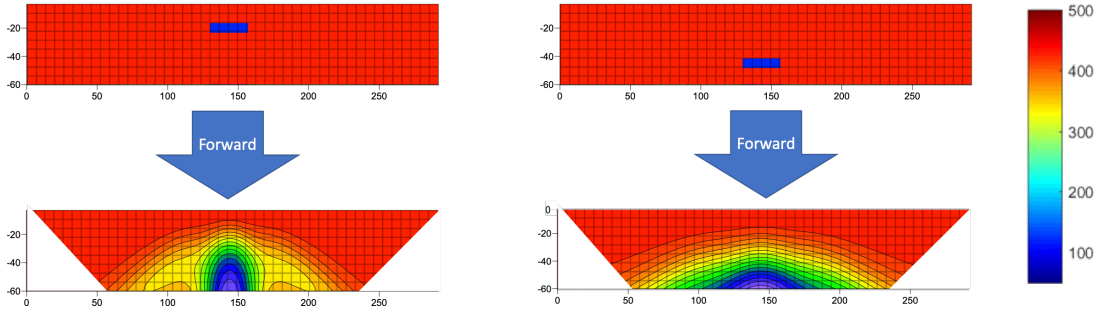


Fig. 2. Two apparent resistivity data and resistivity model pairs. The two resistivity models have the same anomalous bodies but in the different vertical positions. The corresponding patterns of the responses in observed data demonstrate a large difference.

Besides, at present, DNNs have developed many variants with different computational logic, such as Multilayer Perceptrons (MLPs, also known as fully connected networks), convolutional neural networks (CNNs) and recurrent neural networks (RNNs), which further extends the application scenarios.

Many attempts have already verify that DNNs could approximate very complex nonlinear mapping functions, especially for ill-posed inverse problems, such as image super-resolution (Dong *et al.* [31]), medical imaging (Jin *et al.* [32]), and 3D model reconstruction (Choy *et al.* [33]). The successes have also inspired many approaches for geophysical problems, particularly in the field of seismic inversion. Araya-Polo *et al.* [34] use a velocity related feature cube transferred from raw seismic data to generate velocity model by CNNs, while Wu, Lin, and Zhou [35] treat seismic inversion as image mapping and build the mapping from seismic profiles to velocity model directly. Further, Li *et al.* [36] figure out the weak spatial correspondence and the uncertain reflection-reception relationship problems between seismic data and velocity model, and propose to generate spatially aligned features by MLPs at first. The latter two works could build the mapping from raw seismic data to velocity model directly without data pre-processing. All of these works demonstrate promising performance in result accuracy and computation speed, which bring new perspectives for ERS inversion. Besides, by utilizing big data, DNNs based inversion methods are more robust and have the potential of the practical application.

In this paper, deep learning inversion of ERS is to learn the mapping from input (apparent resistivity data) to output (resistivity model) directly by CNNs, which is illustrated in Fig. 1. Typically, the existence of resistivity anomalies in the model will cause responses in apparent resistivity data. Meanwhile, as can be seen from Fig. 1, the responses of observed data caused by different resistivity anomalies also show different patterns, and the patterns demonstrate certain spatial correspondence to resistivity anomalies in the model. Since the patterns are local existing and spatial corresponding to the resistivity anomalies, the input and output can be considered as the natural image, and the task can be treated as the common mapping between images. In this case, CNNs are preferred among a variety of DNNs variants, because they are much powerful in extracting local patterns and more efficiency regards to the number of parameters. And the performance of CNNs has been widely concerned in the research of remote sensing scene (Maggiore *et*

al. [37], Cheng *et al.* [38], Zhang *et al.* [39]). Apart from the similarities with the natural images, apparent resistivity data has its own characteristic. As demonstrated in Fig. 2, when the same anomalous body is located at the different vertical positions, the apparent resistivity data show patterns with large difference, namely patterns have the vertically varying characteristic. This characteristic poses a great challenge for CNNs and may make outputs of CNNs ambiguity. It is because that, with the local spatial and weight sharing convolutional kernels in CNNs, CNNs would have certain receptive field and effective area, and when applying CNNs to the data with vertically varying characteristic, there may be situations where CNNs are requested to give different outputs from similar patterns within effective area. The details will be discussed in Sec. III. This may be the main difficulty for applying CNNs to inverse electrical resistivity data.

We adopt the prevalent CNNs based U-Net architecture [40] to design our networks (ERSInvNet). To capture the potential global resistivity distribution change caused by resistivity anomalies, we set ERSInvNet with 30 layers to have enough receptive fields. Then to reduce the potential ambiguity caused by vertically varying characteristic of apparent resistivity data, we supply ERSInvNet with vertical position information by concatenating an additional tier feature map to the input data. To address the common problem that deep anomalies are difficult to inverse well, we introduce depth weight function in loss function to let network pay more attention to the deep region of resistivity models. Besides, we apply smooth constraints in the loss function to suppress potential false anomalies. In experiments, synthetic examples in our proposed ERSInv dataset are used to verify the feasibility and efficiency, and ERSInvNet is trained end-to-end without any data processing. Through comprehensive qualitative analysis and quantitative comparison, the proposed ERSInvNet consistently achieves promising performance regarding the real-time inference and high inversion accuracy.

II. BACKGROUNDS

The basic measurements of ERS are made by injecting current into the ground through two current electrodes and measuring the potential difference between other pairs of electrodes. In a typical scenario of ERS, the potential difference data are acquired at the Earth's surface as observed data d . The inverse problem involves inferring a set of parameters in model

m from a set of data d , and it usually relies on the minimization of the objective function. Since we achieve resistivity inversion by building the mapping from the observed data to the resistivity model directly through CNNs, the mechanism of CNNs and related concepts are first displayed in this section.

Multilayer perceptrons (MLPs) are the most basic type of neural networks and have been studied for decades that they are sometimes colloquially referred to as "vanilla" neural networks. It consists of many layers of neurons which weight and non-linearly map all inputs from the previous layer to outputs in the current layer. MLPs are a stack of fully connected layers which defined as

$$y_i^l = f(w_i^l y^{l-1} + b_i^l), \quad l = 2 \dots L, \quad (1)$$

where w_i^l denotes the weights in the links from all the neurons in layer $l-1$ (y^{l-1}) to the i -th neuron in layer l (y_i^l) while b_i^l is the corresponding bias. f represents used nonlinear activation function, such as *Sigmoid* and *ReLU* (Maas *et al.* [25]) that

$$\begin{aligned} \text{Sigmoid}(x) &= \frac{1}{1 + \exp^{-x}}, \\ \text{ReLU}(x) &= \max(0, x). \end{aligned} \quad (2)$$

Sigmoid is the most common non-linear activation function. However, it may cause gradient vanish problem as layer increase. Thus, most recent works prefer to use rectified linear activation functions such as *ReLU* which are also more biologically plausible. Nowadays, dozens of non-linear activation functions have been proposed with properties to handle different tasks. According to Hornik [41], even the simplest MLPs that contain three layers of neurons (an input layer, a hidden layer, and an output layer.) could approximate continuous functions on compact subsets of R^n under mild assumptions on the activation function, which is known as Universal approximation theorem. To optimize parameters of networks more efficiently, the back-propagation (BP) algorithm is proposed, it computes the error gradients layer by layer according to the chain rule. Using MLPs is the most direct way to construct the mapping between data of uncertain relationship or with global dependency.

Though MLPs have shown promising performance for many tasks, they are inefficient and impractical to process input with large dimensions, such as images. Usually, the patterns in the images are locally correlated that pixels form the patterns are spatially nearby. Moreover, the patterns in the images are spatially irrelevant that the same pattern may appear in any position. Given these characteristics, CNNs with local spatial and weight sharing convolutional kernels are proposed, which are more efficient and could make the best use of characteristics of natural images. The most basic 2D convolutional operation with 3D inputs in CNNs is defined as:

$$x_{k,i,j}^l = \sum_{c=1}^C \sum_{m=1}^M \sum_{n=1}^N w_{c,m,n}^{l,k} y_{c,i-[M/2]+m,j-[N/2]+n}^{l-1} + b^{l,k} \quad (3)$$

where $w^{l,k}$ is the convolution kernel of size $[C, M, N]$ for layer l and channel k while $b^{l,k}$ is the corresponding bias, and y^{l-1} is the 3D feature map of layer $l-1$ while $x_{k,i,j}^l$ is the

element of position $[k, i, j]$ in convolution results of layer l . It is easy to get that the feature map in layer l is $y^l = f(x^l)$ where f is the non-linear activation function. Please note that Eq. 3 is the most basic 2D convolutional operation with 3D inputs without stride and dilation choice.

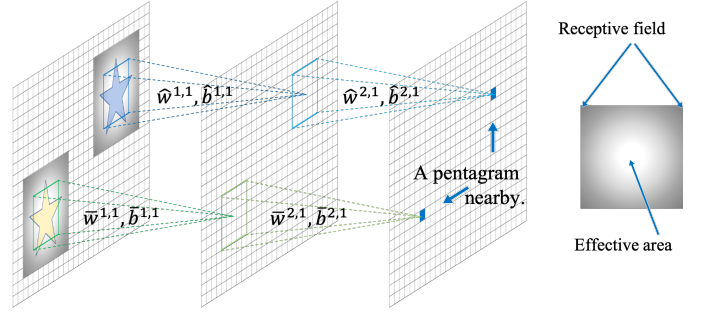


Fig. 3. Illustration of convolutional operation and receptive field concept. The kernel and bias in each layer are weight sharing. The gray area in the input indicates the receptive field caused by two convolutional operations with the 5×5 kernel for elements in the output. The center parts of receptive field (*effective area* [42]) usually have more influence than the surrounding parts and are indicated with light gray color.

A three layers CNNs with only one channel each layer is shown in Fig. 3, the kernel $w^{l,k}$ and the bias $b^{l,k}$ in each layer share the same weight that $\hat{w}^{l,k} = \bar{w}^{l,k}$ and $\hat{b}^{l,k} = \bar{b}^{l,k}$, which is referred to as weight sharing property of CNNs. Modern CNNs are with many convolutional layers, and each layer includes convolution, non-linear activation and some optional operations, such as batchnorm and pooling. Usually, more layers the CNNs have, much stronger the capacity of CNNs is. One rule to decide the number of CNNs' layers is making it at least have enough size of receptive field to cover the whole pattern of the object and meanwhile have enough nonlinear expressiveness. Receptive field is the total number of neighborhood pixels or grids in the image the CNNs consumed to give output. As illustrated in Fig. 2, to classify an image with pentagrams, we concatenate two convolutional layers with 5×5 kernels (stride 1 and dilate 1). In this way, each final output element could have the receptive field of size 7×7 in the input image and thus get aware of the existence of pentagram nearby. Besides, according to Luo *et al.* [42], the center parts of receptive field usually have more influence than the surrounding parts, which is commonly referred to as *effective area*. Certainly, there are many choices to satisfy the requirement of receptive field, and the size of receptive field will be affected by many operations such as pooling and upsampling. As for nonlinear expressiveness of CNNs, it is hard to know whether it enough for the task as the mechanism of CNNs has not been studied comprehensively, so people usually use excessive layers to guarantee the nonlinearity.

III. METHODOLOGY

A. Approach

In this work, we intend to learn the mapping function \mathcal{F} from apparent resistivity data d to resistivity model m directly by DNNs that:

$$m = \mathcal{F}(d) \quad (4)$$

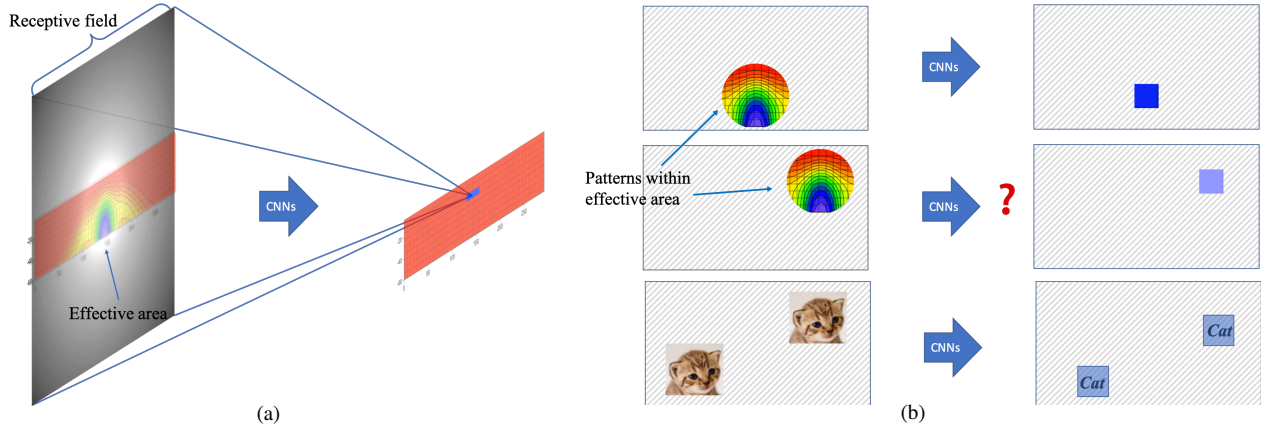


Fig. 4. Illustration of the problem when using CNNs in the raw apparent resistivity data. (a) With deep CNNs, the element in the output will have receptive field cover the whole input data, while the patterns within center parts of receptive field (*effective area* [42]) have much more influence. (b) Different from natural images as shown in the bottom figure, similar patterns within effective area (from the top two figures) may appear at different locations in apparent resistivity data, but with different corresponding model value

As stated in Sec. I, because of patterns shown in apparent resistivity data, our task can be treated as the common image to image mapping where CNNs are much powerful and efficient because of CNNs' weight sharing local convolution kernels. However, with patterns of vertically varying characteristic, CNNs may encounter ambiguous situations. In the following, we will demonstrate and discuss the potential problem when using CNNs on apparent resistivity data.

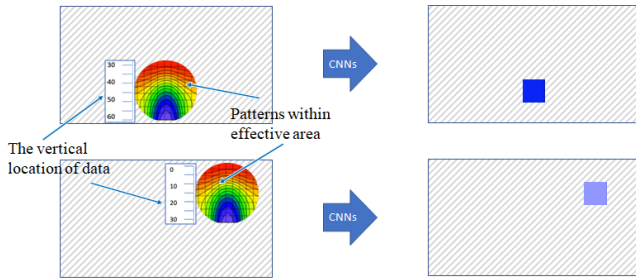


Fig. 5. Illustration of how we reduce the potential ambiguity of CNNs during training. When patterns themselves are distinguishable, we supply them with the corresponding vertical location information to help build the mapping.

Firstly, as illustrated in Fig. 4(a) and proved in Luo *et al.* [42], even using deep CNNs with receptive field cover the whole apparent resistivity data, the patterns within center parts of receptive field usually have much more influence on the corresponding output model value. Thus, the center parts of receptive field are usually referred to as *effective area*. Secondly, due to the definition of apparent resistivity, the patterns within effective area in apparent resistivity data have vertically varying characteristic. There may be situations as shown in the top two figures in Fig. 4(b). The similar patterns within effective area appear at different tier positions, but correspond to different anomalous bodies and model values. Consequently, during training, CNNs may get ambiguous when requested to give different model values from similar input patterns within effective area. As a comparison, for natural images, as the bottom figure in Fig. 4(b) shows, the patterns of cats correspond to the same semantic meaning in

the output no matter where they are located, which means natural images do not have position varying characteristic.

Characteristics of natural images and weight-sharing property of CNNs make CNNs powerful and efficient in dealing with natural images. To make the best use of CNNs in ERS and reduce potential ambiguity, we should supplement input data with more distinguishable information which related to input data, thus reducing the potential ambiguity of CNNs when giving output. In surface ERS, when the distance between two injecting electrodes enlarged, the apparent resistivity data with deeper tier positions in vertical direction could be calculated to achieve the electrical sounding purpose. The data with deeper tier position has the stronger correlation with the deeper anomalous body, which means that the tier position information is helpful for CNNs to distinguish the data patterns caused by anomalous bodies with different depths. Therefore, adding the tier position information of the data to the input would benefit CNNs for building the mapping. As shown in Fig. 5, CNNs could be easier to determine the model values from both patterns and location information together than only rely on possible indistinguishable patterns. Finally, we let CNNs learn the mapping from data and location to model value:

$$m = \mathcal{F}(d, t) \quad (5)$$

where t denotes the tier positions in vertical directions of apparent resistivity data. In the following section, we will detail the architecture of CNNs and how we introduce t .

B. Networks

We design our networks based on prevalently used U-Net architecture (Ronneberger *et al.* [40]) as shown in Fig. 7. U-Net is well known for its shortcut operation which concatenates feature maps from the shallow layer (low-level feature maps) to feature maps from the deep layer (high-level feature maps). Normally, high-level features contain knowledge more related to final result value, while low-level features have knowledge related to some general concepts such as position, shape, etc. In this way, the shortcut would make the last several layers give

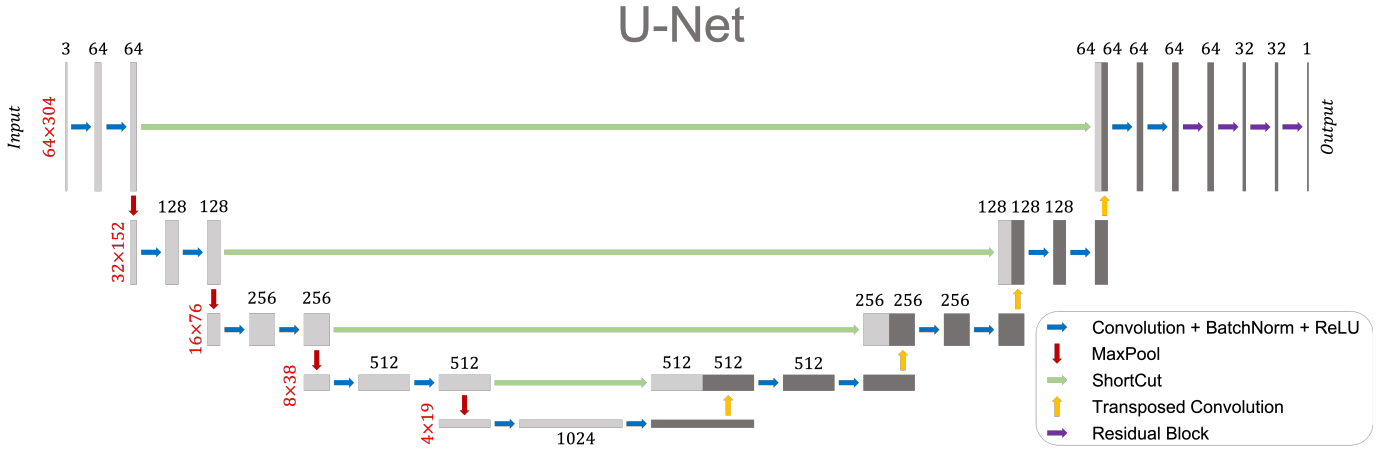


Fig. 6. U-Net architecture. The black number above feature maps indicates the number of channels in feature maps while the red number beside feature maps denotes the spatial dimension of feature maps. Blue arrow represents *Convolution-Batchnorm-ReLU* operation while purple arrow introduces extra residual connection. Red arrow means max-pooling operation which down-samples feature maps while yellow arrow means transposed convolution which up-samples feature maps. Green arrow is the shortcut which concatenates feature maps from shallow layers to deep layers. All the convolution operations are with 3×3 kernel.

outputs based on high-level and low-level knowledge together, so as to help get final results with both accurate value and anomalous morphology. Moreover, the shortcut will help back propagate gradients and accelerate parameter optimization in shallow layers. We also add several residual blocks (He *et al.* [24]) at the end of U-Net to enhance the capacity. Finally, there are 26 layers with convolution operation (3×3 kernel) and nonlinear activation function, and also 4 layers with 2×2 max-pooling operation, which results in enough large receptive field and nonlinearity for our data and task.

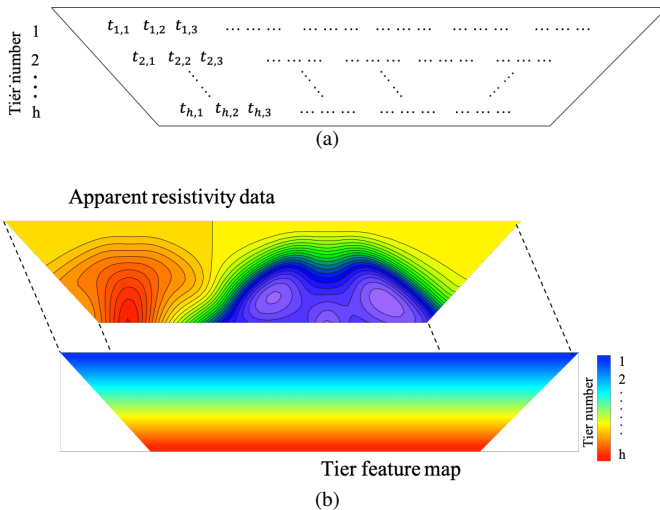


Fig. 7. (a) Tier feature map is with tier structure that element in each tier has the value equal to tier number. (b) Our actual input data after concatenating tier feature map.

To reduce the potential ambiguity when applying CNNs in our task as discussed in previous sections, we introduce tier feature map and concatenate it to the input data to supplement tier position information. In typical surface detection scenarios, the apparent resistivity data with different tier positions in the vertical direction can be obtained by changing the space between injecting electrodes, which is the basic method of

electrical sounding. Under different sounding conditions, the electrodes device moves horizontally along the survey line to form apparent resistivity profile, thereby the data matrix of apparent resistivity could be acquired. In the data matrix of apparent resistivity, the data with different tier positions are strongly correlated with the anomalous structures of corresponding depths. That is to say, introducing tier position information into apparent resistivity data can be regarded as supplementing depth information for CNNs. Our tier feature map is with tier structure that element in each tier has the value equal to tier number, and has the same spatial dimension as d . We denote tier feature map as t and assume d has the height of h , thus t has total h tiers and $t_{i,j} = i$, where i, j indicate vertical and horizontal locations respectively, as shown in Fig. 7(a). Concatenating t to the input data is equivalent to treat t as another channel of the input data, as illustrated in Fig. 7(b).

C. Loss Function

D. Basic Metric and Weighting Function

For value regression problem, we apply prevalently used *MSE* metric for data value term v in loss function. For classical ERS inversion, it is usually more difficult to obtain accurate inversion results for deep anomalies. Li and Oldenburg [43], [44] proposed a weighting function to counteract the natural decay of the static field to overcome the tendency of putting structure at the surface. Its effectiveness has been demonstrated (Kang and Oldenburg [45], Qin *et al.* [46]). In this case, we also take the idea of depth weighting function in loss function to let the network invest more capability in the deep area. In this way, the inversion accuracy and resolution of deep anomalous bodies will be improved. The depth weighting function dw is defined as:

$$dw(\hat{m}_{i,j}) = (i + \lambda)^{\beta/2}, \quad (6)$$

where $\hat{m}_{i,j}$ is the predicted value at position (i, j) of the resistivity model. λ is the constant parameter related to the grid

size and the location of the current electrodes. The parameter β is a constant for controlling depth weight distribution.

Finally, we design our data value term v as

$$v(\hat{m}, m) = \sum_{i,j} dw(\hat{m}_{i,j}) \cdot (\hat{m}_{i,j} - m_{i,j})^2, \quad (7)$$

where \hat{m} is the inverse result by our networks and m is the corresponding ground truth.

E. Smooth Constraints

Inversion tasks are often mathematically ill-posed that the solutions are usually non-unique and unstable. One way to solve this problem is by adopting the well-tested smoothness constrained least-squares approach (Tikhonov *et al.* [47]). Restricted by the smooth constraints, sudden changes between adjacent grids in the resistivity model will be reduced. We carry out the smooth constraints by introducing smooth term:

$$s(\hat{m}) = \sum_{i,j} |\hat{m}_{i+1,j} - \hat{m}_{i,j}| + |\hat{m}_{i,j+1} - \hat{m}_{i,j}|. \quad (8)$$

Smooth term plays the role of regularization and is also known as total variation loss.

F. Final Formulation

Consequently, our final loss function L is defined as

$$L = v(\hat{m}, m) + \alpha \cdot s(\hat{m}) \quad (9)$$

where α is the smoothness factor. All the operations and losses are derivable and result in our end-to-end networks which we call ERSInvNet.

IV. EXPERIMENTS

A. Dataset Preparation

For deep learning based geophysical inversion, data set generally should reach a sufficient amount and guarantee the diversity. As such, in our work, we collect a dataset with 36,214 pairs of different resistivity model and corresponding apparent resistivity data, which is called ERSInv Dataset. Resistivity model is designed by referring to real 2-D ERS scenarios. We generate synthetic data by predefining a few anomalous bodies with different resistivity value, and then embedding them to the different positions of homogeneous medium (500 $\Omega \cdot m$). The resistivity anomalous bodies consist of 5 subsets as follows. *Type I*: Single rectangular body (5236 sample pairs), *Type II*: Two rectangular bodies (7,560 sample pairs), *Type III*: Three rectangular bodies (7,920 sample pairs), *Type IV*: Single declining bodies (6,426 sample pairs) and *Type V*: Two declining bodies (9,072 sample pairs). For each type, the resistivity anomalous bodies may have different resistivity values, in our dataset low resistivity anomaly is the one with body value from [10 $\Omega \cdot m$, 20 $\Omega \cdot m$, 50 $\Omega \cdot m$] and high resistivity anomaly is the one with body value from [1000 $\Omega \cdot m$, 1500 $\Omega \cdot m$, 2000 $\Omega \cdot m$]. Accordingly, we have total five different types of resistivity models and the corresponding apparent resistivity data are generated by forward modeling. Schematic diagram and parameters of anomalous bodies are shown in Tab. I.

The selection of electrode configuration for the ERS is crucial in acquiring the response of the observed target because different electrode configurations have different horizontal and vertical resolution [48]. The apparent resistivity data of Wenner and Wenner-Schlumberger arrays are adopted in this work since these two configurations will have good vertical resolution and appropriate horizontal resolution (Sasaki [49], Szalai *et al.* [50]) when they used together. Our observation data are generated through forward modeling on resistivity models.

The simulated electrical fields are usually generated by finite-element methods based on anomalous potential method. The values of both input and output during training are normalized to the range of [0, 1] since standardizing either input or target variables tend to make the training process better behaved (El-Qady and Ushijima [19]). With tier feature map proposed in the last section, each input data will have three channels with two channels of apparent resistivity data and one channel of tier feature map. The dataset is randomly divided into training set, validation set and test set in a ratio of 10 : 1 : 1 (training set: 30,180 pairs; validation set: 3,017 pairs; test set: 3,017 pairs).

B. Implementation

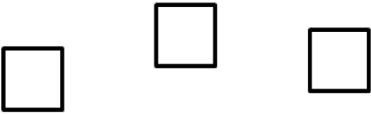
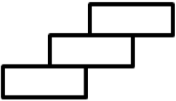
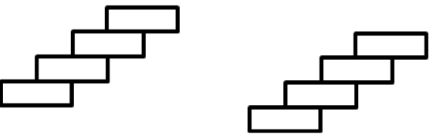
The neural networks in this work are built using PyTorch. SGD optimizer with batchsize 5, learning rate 0.1, momentum 0.9 and weight decay $1e-4$ is used to optimize networks. During training, we carry out 500 epochs of optimization in total, and also perform one time of validation after each training epoch to verify training effect. The parameters β and λ of depth weighting function are set to be 1 and 8 respectively, and the smoothness factor α is set to be 0.2. In this work, the hyper-parameters such as β , λ and α are chosen according to the evaluation on the validation set. All computations are carried out with the machine of single NVIDIA TITAN Xp. It is worth to note that in this environment, our ERSInvNet could reach real-time inference during testing with 0.013s/data.

In order to verify the proposed ERSInvNet, four experiments are arranged as follows: *Experiment 1*, ERSInvNet performance analysis; *Experiment 2*, the ablation study of tier feature map; *Experiment 3*, the ablation study of depth weighting function and smooth regularization; *Experiment 4*, comparison of ERSInvNet and linear least squares inversion. In addition to qualitative evaluation through visual judgment, weighted mean square error (WMSE) and weighted correlation coefficient (WR) are also used to measure the performance quantitatively, which is given as follows:

$$\begin{aligned} WMSE &= \frac{1}{N} \sum_{n=1}^N [w^n(\hat{m}^n - m^n)]^T [w^n(\hat{m}^n - m^n)] \\ WR &= \frac{1}{N} \sum_{n=1}^N \frac{[w^n \circ (\hat{m}^n - \tilde{m}^n)]^T [w^n \circ (m^n - \tilde{m}^n)]}{|w^n \circ (\hat{m}^n - \tilde{m}^n)|_2 |w^n \circ (m^n - \tilde{m}^n)|_2} \end{aligned} \quad (10)$$

where m^n and \hat{m}^n are vectorized actual and predicted model values respectively while w^n is the vectorized weight, and we use $\tilde{\cdot}$ to denote the average values of \cdot . w^n is designed to make the region far from anomalies in the resistivity model has large

TABLE I
SCHEMATIC DIAGRAM AND PARAMETERS OF ANOMALOUS BODIES.

	<ul style="list-style-type: none"> •Type I: Single rectangular body •Model quantity: 5236 pairs •Anomalous bodies size : 4×4; 6×6; 8×8; 10×10; 12×12; 14×14; 16×16; 18×18; 20×20; 8×30; 20×10 •Anomalous bodies types: 1 low resistivity body; 1 high resistivity body
	<ul style="list-style-type: none"> •TypeII: Two rectangular body •Model quantity: 7560 pairs •Anomalous bodies size : 8×8; 10×10; 8×30; 20×10 •Anomalous bodies types: 2 low resistivity bodies; 2 high resistivity bodies; 1 low resistivity body & 1 high resistivity body
	<ul style="list-style-type: none"> •TypeIII: Three rectangular body •Model quantity: 7920 pairs •Anomalous bodies size : 8×8; 10×10; 8×30; 20×10 •Anomalous bodies types: 3 low resistivity bodies; 3 high resistivity bodies; 1 low resistivity body & 2 high resistivity body; 2 low resistivity body & 1 high resistivity body
	<ul style="list-style-type: none"> •Type IV: Single declining body •Model quantity: 6426 pairs •Anomalous bodies size : 8×4; 10×5; 12×6 layer: 3; 4; 5 •Anomalous bodies types: 1 low resistivity body; 1 high resistivity body
	<ul style="list-style-type: none"> •Type V: Two declining body •Model quantity: 9072 pairs •Anomalous bodies size : 8×4; 12×6 layer: 4; 5 •Anomalous bodies types: 2 low resistivity bodies; 2 high resistivity bodies; 1 low resistivity body & 1 high resistivity body

weight, because false anomalies far from true anomalies are not preferred, while false anomalies closed to true anomalies are usually acceptable. N is the number of samples. $WMSE$ measures the value fitting between prediction and groundtruth with the value the lower the better, while WR measures the statistical relationship between prediction and groundtruth with the value the larger the better and value range in $[0, 1]$.

V. RESULTS AND DISCUSSION

A. Results of Experiment 1

In Experiment 1, some examples will be shown to demonstrate the inversion performance of the proposed method. The misfit degree of locations and shapes of anomalous bodies as well as resistivity values are the major factors considered during evaluation. In Fig. 8, we randomly select five inversion results which correspond to five model types respectively in the test set. The images arranged from left to right are the corresponding ground truth, apparent resistivity data, ERSInvNet results and the vertical resistivity profiles, respectively.

From the first two columns, we can notice that spatial correspondence extensively exists between the apparent resistivity data and the resistivity models. From the overall observation of Fig. 8, ERSInvNet could predict model value accurately and also get good localization of anomalous bodies, which demonstrates its promising inversion ability. In order

to visualize the positions, shapes and resistivity values of anomalous bodies in inversion results more intuitively, the resistivity change along anomalous body profile (shown by the black line in Fig. 8) is given in the form of curves on the fourth column. We can see that the resistivity curves of inversion results and models are almost aligned (with the error within 0.4 %) and change synchronously in most places except regions near the boundary of the anomalous bodies. This is because that the smooth constraints restrict the mutation of resistivity value near abnormal body boundary. The effect of smooth constraints will be discussed in the Sec. V-C.

In the third example, three anomalous bodies with different depths can be clearly and accurately reflected in the inversion results. Among them, the high resistivity bodies at the depth of 15 m and 25 m are closed to the model value, while the resistivity of the deepest one (with value 400 $\Omega \cdot m$) is lower than the background (with value 2000 $\Omega \cdot m$). The reason is that when powered on the surface, the field responses caused by deep anomaly have not shown obvious patterns in the apparent resistivity data. The lack of obvious pattern makes ERSInvNet hard to give accurate predictions. Besides, the inversion results show interesting phenomena that boundary description of high resistivity body is more accurate than that of low resistivity body. More examples from the validation and test sets are shown in the supplementary for further comparison.

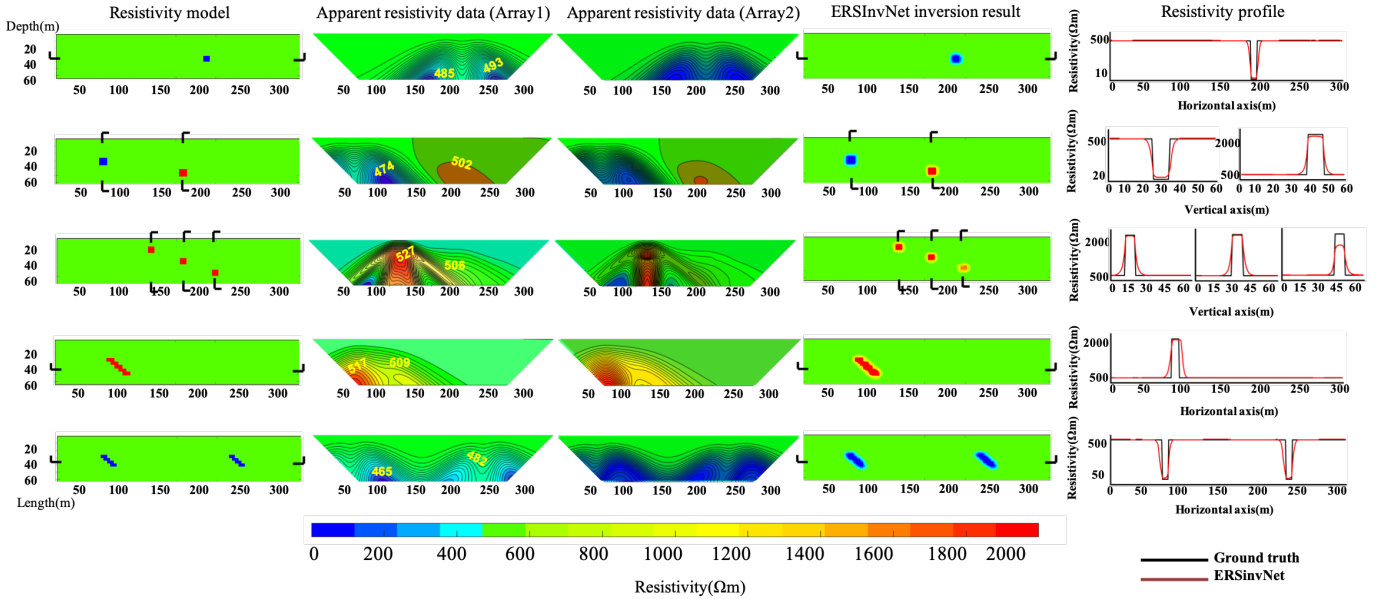


Fig. 8. Ground truth (the first column), inversion results of our ERSInvNet (the fourth column) and corresponding apparent resistivity data (the second and third column) on the test set. Vertical and horizontal profiles of resistivity models indicated by the truncation line are shown in the rightmost column for comparing the inverted resistivity values. Rows from top to bottom exhibit examples with the anomalous bodies from *type I-V*, respectively.

In Fig. 9, we show the loss curves of our ERSInvNet on the training and validation set respectively. Both loss curves decrease gradually with the increase of epochs, which indicates the non-existence of over-fitting during training. When the epochs reached 500 times, the loss was reduced below 0.001 and the trend of decline seems will continue.

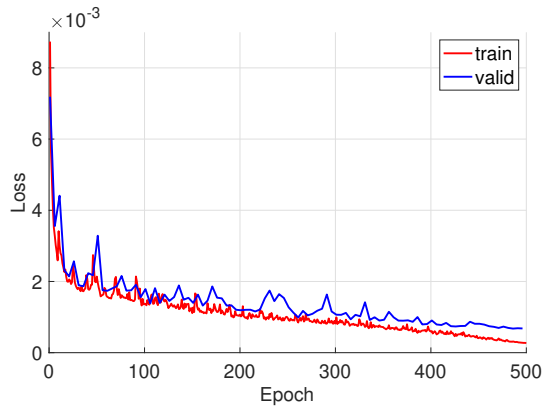


Fig. 9. Loss curves for ERSInvNet on training and validation sets.

B. Results of Experiment 2

In Experiment 2, to verify the role of tier feature map, we compare the ERSInvNet results with/without the tier feature map when having both depth weighting function and smooth constraints in the loss function. Examples with five different types of anomalous bodies are randomly selected. Inversion results with/without tier feature map are shown in Fig. 10. From example 1, example 2 and low resistivity body on the right side of example 5, we can see the supplement of tier information helps improve the morphological accuracy when inverse resistivity anomalies. Also, the delineation of the

boundaries of anomalous bodies is also improved. In example 2 and 3, for multiple anomalous bodies, the tier feature map helps suppress the obvious false anomalies near true ones. Specifically, in example 2, the false anomalies around the low resistivity anomalous body are removed after introducing tier feature map, meanwhile the shape of the anomalous body is more accurate. Similarly, three obvious high resistivity false anomalies in example 3 are completely removed. Without tier feature map, using CNNs on data with vertically varying characteristic will cause ambiguity as discussed in Sec. III, and give many assumptions to make loss function lower which finally results in false anomalies. (It is worth to note that what the possible results the networks guessed look like depends on what samples the networks learn during training.)

In summary, the tier feature map can suppress false anomalies. Such rules generally exist in other results. To check the overall performance on validation and test sets, we quantitatively compare results by MAE and R^2 metrics in Table. II. It is easy to get that quantitative evaluation also supports the positive effect of the tier feature map. Certainly, besides the effects of tier feature map, the inversion performance also depends on the contribution of our smooth constraints and depth weighting function, which will be discussed in the next subsection.

C. Results of Experiment 3

In experiment 3, we compare the results with/without smooth constraints and depth weighting function when having tier feature map in the input data. Thus, we have four configurations in total that with smooth constraint and depth weighting function together (SD), with only smooth constraint (OS), with only depth weighting function (OD) and with nothing (NA).

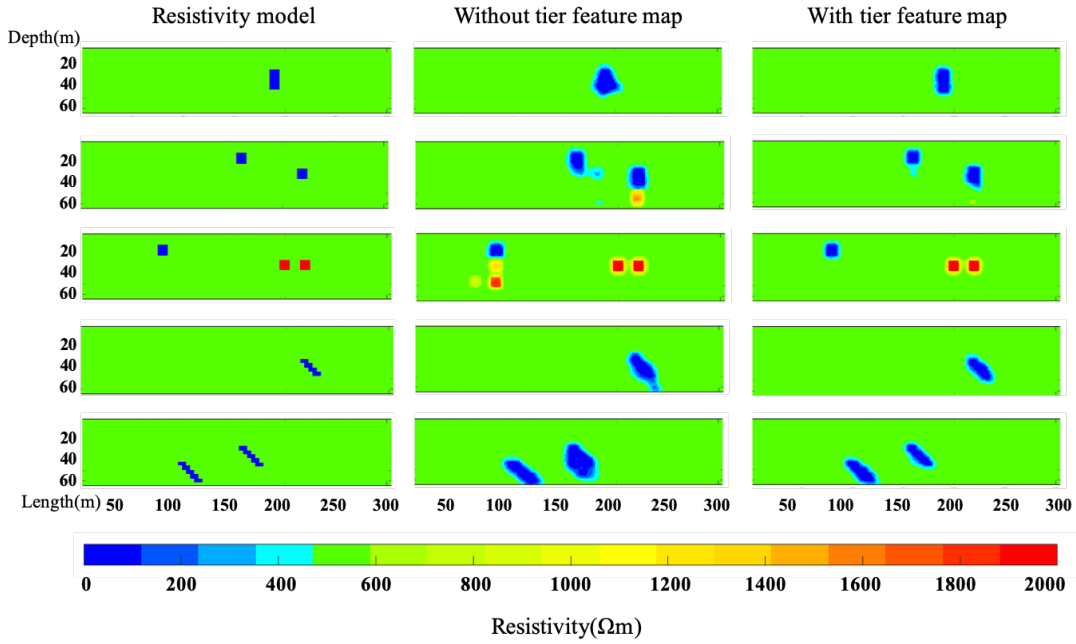


Fig. 10. ERSInvNet inversion results with/without tier feature map on the test set. Rows from top to bottom exhibit examples with the anomalous bodies from *type I-V*, respectively. The comparison in this figure indicates that the tier feature map has positive effects on the inversion accuracy.

TABLE II

TABLE II QUANTITATIVE COMPARISON OF INVERSION RESULTS WITH/WITHOUT DEPTH FEATURE MAP ON TEST AND VALIDATION SETS. THE \uparrow INDICATES THE LARGER VALUE ACHIEVED, THE BETTER PERFORMANCE IS, WHILE \downarrow INDICATES THE SMALLER, THE BETTER.

	Test		Valid	
	MSE \downarrow	R ² \uparrow	MSE \downarrow	R ² \uparrow
With tier feature map	0.000335	0.540852	0.000341	0.538876
Without tier feature map	0.000731	0.387227	0.000721	0.385944

TABLE III

TABLE III QUANTITATIVE COMPARISON OF INVERSION RESULTS WITH/WITHOUT SMOOTH CONSTRAINTS AND DEPTH WEIGHTING FUNCTION ON TEST AND VALIDATION SETS. THE \uparrow INDICATES THE LARGER VALUE ACHIEVED, THE BETTER PERFORMANCE IS, WHILE \downarrow INDICATES THE SMALLER, THE BETTER.

	Test		Valid	
	MSE \downarrow	R ² \uparrow	MSE \downarrow	R ² \uparrow
SD	0.000335	0.540852	0.000341	0.538876
OD	0.000608	0.387756	0.000592	0.387921
OS	0.000959	0.335904	0.000971	0.335029
NA	0.000549	0.425744	0.000555	0.421256

In Fig. 11, resistivity models and inversion results of *NA*, *OS*, *OD* and *SD* are given from left to right.

By comparing the results of *NA* and *OS*, we see the results with smooth constraints have fewer false anomalies but poor boundary accuracy. (See the second and third columns). By comparing *NA* and *OD*, we found results with depth weighting function have more accurate anomaly morphology as well as anomaly value, especially in the deep area. That is to say, the main contribution of smooth constraints is to suppress false anomalies, while depth weighting function will benefit inversion accuracy. The overall comparison indicates that ERSInvNet with all the tier feature map, smooth constraints and depth weighting function (*SD*) has the best performance.

MSE and *R*² scores of four different ERSInvNet configurations on validation and test sets are listed in Tab. III. On the whole, *SD* has the highest *R*² as well as lowest *MES* value, which is consistent with the results of the visual comparison. However, *OD* and *OS* are unexpected even worse than *NA* after introducing smooth constraints and depth weighting function respectively. Especially, when smooth constraints are applied in *OS*, the *MSE* increases by 74.7 % which means smooth constraints would sacrifice much accuracy for delineating the boundaries of anomalies. For the performance decrease

of applying depth weighting function, we guess it may be caused by the overproduced false anomalies in the deep area. With depth weighting function, to avoid missing detection of anomalies in the deep area and causing high loss, networks may make many assumptions which result in false anomalies. After introducing smooth constraints and depth weighting function together (*SD*), we got the best performance which indicates that smooth constraints and depth weighting function can mutually benefit and restrain the negative effects.

D. Results of Experiment 4

In Experiment 4, we benchmark ERSInvNet against the well-known iterated linear inversion using *RES2DINV* software which is widely applied in ERS inversion. For a fair comparison, we use synthetic model with position, size and resistivity value of anomalies that unprecedented during the training of our ERSInvNet. And the same configuration are used to generate corresponding resistivity data for both methods. Fig. 12 (b) and (c) show the results of the linear method and our proposed ERSInvNet respectively. The results of both methods can depict the existence of the anomalous bodies, but

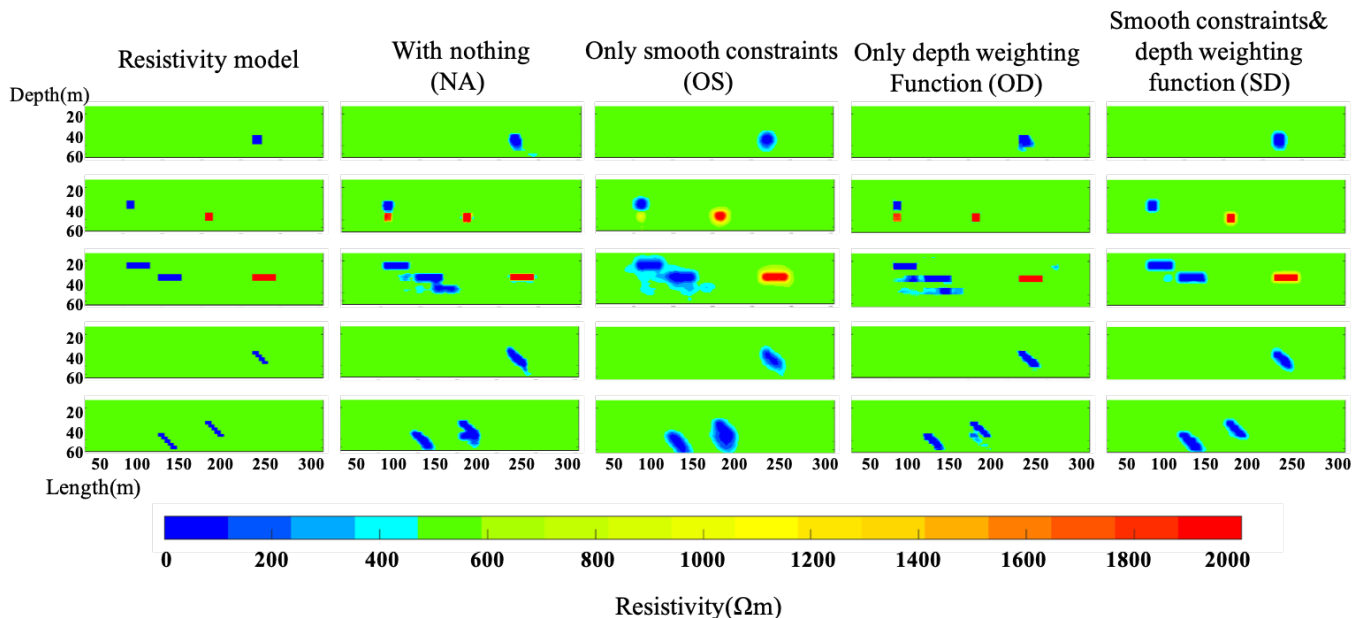


Fig. 11. Inversion results on different configurations on the validation and test sets. Rows from top to bottom exhibit examples with the anomalous bodies from *type I-V*, respectively. The comparison indicates that the smooth constraints could suppress false anomalies and depth weighting function benefits the inversion accuracy.

the ERSInvNet predicts the location, shape of the conductive block and the resistivity value more precisely than the linear method. Compared with traditional methods, DNNs based methods could utilize data prior learned from the training set as well as human-introduced priors such as smoothness, meanwhile they have more powerful nonlinear approximation abilities. With all these advantages, DNNs reach these promising results in our task.

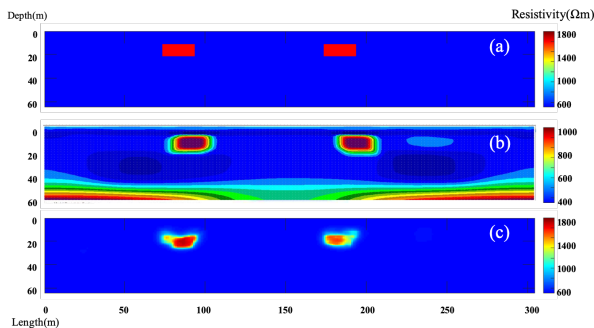


Fig. 12. Synthetic example and inversion results. (a) synthetic model, (b) inversion results of the proposed ERSInvNet, (c) inversion results of the linear method.

VI. CONCLUSIONS

In this paper, we propose a CNNs based network called ERSInvNet for inverse problems on resistivity data. Though some attempts of CNNs based tomography have been made, ERS inversion is different from the previous studies because of the vertically varying characteristic inherent in apparent resistivity data. This characteristic will lead to ambiguity when using CNNs directly. To address this issue, we supplement a tier feature map to the input data. Besides, to further reduce the false anomalies and improve the prediction accuracy for the

deep region, smooth constraints and depth weighting function are introduced into loss function during training.

To train, validate and test the proposed ERSInvNet, we collect a dataset that contains 36,214 pairs of apparent resistivity data and resistivity model. Comparative experiments show that including the tier feature map helps to obtain more accurate inversion results and suppress false anomalies. The individually use of smooth constraints and depth weighting function can reduce false anomalies or improve prediction accuracy for the deep region. However it will sacrifice performance in other aspects. Through comprehensive qualitative analysis and quantitative comparison, simultaneously use of both them achieves the best results. Moreover, comparing with traditional methods, ERSInvNet could reach real-time inference during testing. In future research, we will focus on the establishment of a general dataset covering typical geological conditions and the application of field data.

VII. ACKNOWLEDGMENTS

This work was supported by the grants of National Natural Science Foundation of China (No. 51739007, 61702301), the United Fund of National Natural Science Foundation of China (U1806226), Development Program of China (No. 2016YFC0401805), Key Research and Development Plan of Shandong Province (Z135050009107), the Interdiscipline Development Program of Shandong University (No. 2017JC002) and Fundamental Research Funds of Shandong University.

REFERENCES

- [1] M. Loke, J. Chambers, D. Rucker, O. Kuras, and P. Wilkinson, "Recent developments in the direct-current geoelectrical imaging method," *Journal of Applied Geophysics*, vol. 95, pp. 135–156, 2013.
- [2] D. LaBrecque, A. Ramirez, W. Daily, A. Binley, and S. Schima, "Ert monitoring of environmental remediation processes," *Measurement Science and Technology*, vol. 7, no. 3, pp. 375–385, 1996.

- [3] K. Hayley, L. Bentley, and M. Gharibi, "Time-lapse electrical resistivity monitoring of salt-affected soil and groundwater," *Water Resources Research* 45, W07425, 2009.
- [4] J. Reynolds, "An introduction to applied and environmental geophysics, 2nd edition," *John Wiley & Sons*, 2011.
- [5] J. Kim, M. Yi, Y. Song, S. Seol, and K. Kim, "Application of geophysical methods to the safety analysis of an earth dam," *Journal of Environmental and Engineering Geophysics*, vol. 12, no. 2, pp. 221–235, 2007.
- [6] P. Wilkinson, J. Chambers, P. Meldrum, D. Gunn, R. Ogilvy, and O. Kuras, "Predicting the movements of permanently installed electrodes on an active landslide using time-lapse geoelectrical resistivity data only," *Geophysical Journal International*, vol. 183, no. 2, pp. 543–556, 2010.
- [7] P. Sjudahl, T. Dahlin, and S. Johansson, "Using the resistivity method for leakage detection in a blind test at the rossvatn embankment dam test facility in norway," *Bulletin of Engineering Geology and the Environment*, vol. 69, no. 4, pp. 643–658, 2010.
- [8] S. Park, "Fluid migration in the vadose zone from 3-d inversion of resistivity monitoring data," *Geophysics*, vol. 63, no. 1, pp. 41–51, 1998.
- [9] L. Slater and A. Binley, "Evaluation of permeable reactive barrier (prb) integrity using electrical imaging methods," *Geophysics*, vol. 68, no. 3, pp. 911–921, 2003.
- [10] D. Rucker, "A coupled electrical resistivity-infiltration model for wetting front evaluation," *Vadose Zone Journal*, vol. 8, no. 2, pp. 383–388, 2009.
- [11] S. Cho, H. Jung, H. Lee, H. Rim, and S. K. Lee, "Real-time underwater object detection based on dc resistivity method," *IEEE Transactions on Geoscience and Remote Sensing*, vol. 54, no. 11, pp. 6833–6842, 2016.
- [12] J. Legault, D. Carriere, and L. Petrie, "Synthetic model testing and distributed acquisition dc resistivity results over an unconformity uranium target from the athabasca basin, northern saskatchewan," *The Leading Edge*, vol. 27, no. 1, pp. 46–51, 2008.
- [13] J. Chambers, P. Wilkinson, D. Wardrop, A. Hameed, I. Hill, C. Jeffrey, M. Loke, P. Meldrum, O. Kuras, M. Cave, and D. Gunn, "Bedrock detection beneath river terrace deposits using three-dimensional electrical resistivity tomography," *Geomorphology*, pp. 17–25, 2012.
- [14] X. Liu, F. Liu, J. Chen, Z. Zhao, A. Wang, and Z. Lu, "Resistivity logging through casing response of inclined fractured formation," *IEEE Transactions on Geoscience and Remote Sensing*, vol. 56, no. 8, pp. 4919–4929, 2018.
- [15] C. Schwarzbach, R.-U. Borner, and K. Spitzer, "Two-dimensional inversion of direct current resistivity data using a parallel, multi-objective genetic algorithm," *Geophysical Journal International*, pp. 685–695, 2005.
- [16] B. Liu, S. Li, L. Nie, J. Wang, X. L., and Q. Zhang, "3d resistivity inversion using an improved genetic algorithm based on control method of mutation direction," *Journal of Applied Geophysics*, vol. 87, no. 12, pp. 1–8, 2012.
- [17] S. P. Sharma, "Vfsares-a very fast simulated annealing fortran program for interpretation of 1-d dc resistivity sounding data from various electrode arrays," *Computers & Geosciences*, pp. 177–188, 2012.
- [18] R. Shaw and S. Srivastava, "Particle swarm optimization: A new tool to invert geophysical data," *Geophysics*, vol. 72, pp. 75–83, 2007.
- [19] G. El-Qady and K. Ushijima, "Inversion of dc resistivity data using neural networks," *Geophysical Prospecting*, vol. 49, pp. 417–430, 2001.
- [20] A. Neyamadpour, W. W. Abdullah, S. Taib, and D. Niamadpour, "3d inversion of dc data using artificial neural networks," *Studia Geophysica Et Geodaetica*, vol. 54, pp. 465–485, 2010.
- [21] S. Maiti, V. C. Erram, G. Gupta, and R. K. Tiwari, "Ann based inversion of dc resistivity data for groundwater exploration in hard rock terrain of western maharashtra (india)," *Journal of Hydrology*, 2012.
- [22] F. Jiang, L. Dong, and Q. Dai, "Electrical resistivity imaging inversion: An isfla trained kernel principal component wavelet neural network approach," *Neural Networks*, vol. 104, pp. 114–123, 2018.
- [23] M. Al-Abri and N. Hilal, "Artificial neural network simulation of combined humic substance coagulation and membrane filtration," *Chemical Engineering Journal*, vol. 141, pp. 27–34, 2008.
- [24] K. He, X. Zhang, S. Ren, and J. Sun, "Deep residual learning for image recognition," in *The IEEE Conference on Computer Vision and Pattern Recognition (CVPR)*, June 2016.
- [25] A. L. Maas, A. Y. Hannun, and A. Y. Ng, "Rectifier nonlinearities improve neural network acoustic models," in *ICML Workshop on Deep Learning for Audio, Speech and Language Processing*, 2013.
- [26] S. Ioffe and C. Szegedy, "Batch normalization: Accelerating deep network training by reducing internal covariate shift," in *Proceedings of the 32nd International Conference on Machine Learning*, 2015.
- [27] Y. LeCun, Y. Bengio, and G. E. Hinton, "Deep learning," *Nature*, vol. 521, no. 7553, pp. 436–444, 2015.
- [28] A. Krizhevsky, I. Sutskever, and G. E. Hinton, "Imagenet classification with deep convolutional neural networks," in *Advances in Neural Information Processing Systems* 25. Curran Associates, Inc., 2012, pp. 1097–1105.
- [29] K. Simonyan and A. Zisserman, "Very deep convolutional networks for large-scale image recognition," *arXiv:1409.1556*, 2014.
- [30] P. Jiang, F. Gu, Y. Wang, C. Tu, and B. Chen, "Difnet: Semantic segmentation by diffusion networks," in *Advances in Neural Information Processing Systems* 31. Curran Associates, Inc., 2018.
- [31] C. Dong, C. C. Loy, K. He, and X. Tang, "Image super-resolution using deep convolutional networks," *IEEE transactions on pattern analysis and machine intelligence*, vol. 38, no. 2, pp. 295–307, 2016.
- [32] K. H. Jin, M. T. McCann, E. Froustey, and M. Unser, "Deep convolutional neural network for inverse problems in imaging," *IEEE Transactions on Image Processing*, vol. 26, no. 9, pp. 4509–4522, 2017.
- [33] C. B. Choy, D. Xu, J. Gwak, K. Chen, and S. Savarese, "3d-r2n2: A unified approach for single and multi-view 3d object reconstruction," in *Proceedings of the European Conference on Computer Vision (ECCV)*, 2016.
- [34] M. Araya-Polo, J. Jennings, A. Adler, and T. Dahlke, "Deep-learning tomography," *The Leading Edge*, vol. 37, no. 1, pp. 58–66, 2018.
- [35] Y. Wu, Y. Lin, and Z. Zhou, "Inversionnet: Accurate and efficient seismic waveform inversion with convolutional neural networks," in *SEG Technical Program Expanded Abstracts 2018*. Society of Exploration Geophysicists, 2018, pp. 2096–2100.
- [36] S. Li, B. Liu, Y. Ren, Y. Chen, S. Yang, Y. Wang, and P. Jiang, "Deep learning inversion of seismic data," *arXiv:1901.07733*, 2019.
- [37] E. Maggiori, Y. Tarabalka, G. Charpiat, and P. Alliez, "Convolutional neural networks for large-scale remote-sensing image classification," *IEEE Transactions on Geoscience and Remote Sensing*, vol. 55, no. 2, pp. 645–657, 2017.
- [38] G. Cheng, C. Yang, X. Yao, L. Guo, and J. Han, "When deep learning meets metric learning: Remote sensing image scene classification via learning discriminative cnns," *IEEE Transactions on Geoscience and Remote Sensing*, vol. 56, no. 5, pp. 2811–2821, 2018.
- [39] Q. Zhang, Q. Yuan, C. Zeng, X. Li, and Y. Wei, "Missing data reconstruction in remote sensing image with a unified spatial-temporal-spectral deep convolutional neural network," *IEEE Transactions on Geoscience and Remote Sensing*, vol. 56, no. 8, pp. 4274–4288, 2018.
- [40] O. Ronneberger, P. Fischer, and T. Brox, "U-net: Convolutional networks for biomedical image segmentation," in *Medical Image Computing and Computer-Assisted Intervention – MICCAI 2015*, 2015.
- [41] K. Hornik, "Approximation capabilities of multilayer feedforward networks," *Neural Networks*, vol. 4, no. 2, pp. 251–257, 1991.
- [42] W. Luo, Y. Li, R. Urtasun, and R. Zemel, "Understanding the effective receptive field in deep convolutional neural networks," in *Advances in Neural Information Processing Systems* 29, 2016, pp. 4898–4906.
- [43] Y. Li and D. Oldenburg, "3-d inversion of magnetic data," *Geophysics*, vol. 61, no. 2, pp. 394–408, 1996.
- [44] —, "3-d inversion of gravity data," *Geophysics*, vol. 63, no. 1, pp. 109–119, 1998.
- [45] S. Kang and D. Oldenburg, "On recovering distributed ip information from inductive source time domain electromagnetic data," *Geophysical Journal International*, vol. 207, no. 1, pp. 174–196, 2016.
- [46] P. Qin, D. Huang, Y. Yuan, M. Geng, and J. Liu, "Integrated gravity and gravity gradient 3d inversion using the non-linear conjugate gradient," *Journal of Applied Geophysics*, vol. 126, pp. 52–73, 2016.
- [47] T. A.N., G. A.V., S. V.V., and Y. A.G., *Numerical Methods for the Solution of Ill-posed Problems*. Kluwer Academic Publisher, 1995.
- [48] B. Zhou and S. Greenhalgh, "Cross-hole resistivity tomography using different electrode configurations," *Geophysical Prospecting*, vol. 48, no. 5, pp. 887–912, 2000.
- [49] Y. Sasaki, "Resolution of resistivity tomography inferred from numerical simulation," *Geophysical Prospecting*, vol. 40, pp. 453–464, 1992.
- [50] S. Szalai and L. Szarka, "On the classification of surface geoelectric arrays," *Geophysical Prospecting*, vol. 56, no. 8, pp. 4274–4288, 2008.